# Mechanical and Structural Transformations of Tungsten Implanted with Helium Ions

M. Balooch<sup>1</sup>, F. I. Allen<sup>2, 3</sup>, M. P. Popovic<sup>1</sup> and P. Hosemann<sup>1, 4\*</sup>

## Abstract

The near-surface structural and mechanical changes of tungsten upon exposure to 25 keV helium ions at doses ranging from  $1\times10^2$  to  $1\times10^4$  ions/nm² ( $1\times10^{16}$  to  $1\times10^{18}$  ions/cm²) are investigated using site-specific implantation, imaging and probing techniques. Helium Ion Microscopy and Atomic Force Microscopy are used to investigate surface topography changes due to swelling and blistering, and nanoindentation is used to study changes in material hardness. An analytical model has been developed to qualitatively explain bubble formation, surface swelling and the variation in local hardness with depth observed experimentally. The model assumes that the implanted helium has a Gaussian depth distribution, which the helium nanobubbles also follow due to their fast formation. There are two competing processes proposed: (1) a reduction in hardness due to the decrease in material density from bubble formation, and (2) an increase in hardness due to bubbles acting as pinning points that impede dislocation motion.

## 1. Introduction

Nuclear fusion exposes materials such as plasma-facing components to extraordinary environments. Hydrogen isotopes [1] and helium with energies ranging from 10 eV to several keV, combined with neutrons, induce near-surface irradiation degradation of materials exposed to the plasma [2]. The degradation typically starts with the creation of point defects such as vacancies and interstitials, followed by diffusion and recombination processes. These processes produce clusters and cavities (bubbles and voids), and finally microscopic or macroscopic defects (such as fuzz formation [1], blistering and cracking [2]), eventually resulting in catastrophic failure of the material. Body-centered cubic (bcc) materials have generally been shown to exhibit high radiation damage tolerance. Tungsten in particular, with its superior chemical, thermal and mechanical properties, has been designated as one of the primary candidates for the plasma-facing material in fusion reactor design [3, 4].

Radiation-damage-induced cavities and blister formation have been the subject of numerous investigations for many decades [5-7]. Nelson [8] was among the first to report nanobubble formation in experiments at room temperature using 60 keV helium ion irradiation. This was followed by Bauer and Thomas [9], who investigated blister formation on palladium bombarded

<sup>&</sup>lt;sup>1</sup> Department of Nuclear Engineering, University of California Berkeley, Berkeley, CA 94720–1730

<sup>&</sup>lt;sup>2</sup> Department of Materials Science and Engineering, University of California Berkeley, Berkeley CA 94720, USA

<sup>&</sup>lt;sup>3</sup> National Center for Electron Microscopy, Molecular Foundry, Lawrence Berkeley National Laboratory, Berkeley, CA 94720, USA

<sup>&</sup>lt;sup>4</sup> Materials Sciences Division, Lawrence Berkeley National Laboratory, Berkeley CA 94720, USA

<sup>\*</sup>Corresponding author: peterh@berkeley.edu

with 300 keV helium ions at 93 K. Blistering on molybdenum was reported by Erents and McCracken [10] using helium ions at energies up to 80 keV at room temperature. A critical dose of  $5\times10^3$  ions/nm<sup>2</sup> for the onset of blistering was determined. In addition, blister size was found to increase linearly with ion energy.

Irradiation of tungsten with helium and deuterium ions at high temperatures was investigated by Cipiti and Kulcinski [11], determining that above 1000 K, porous surface structures were formed by 30 keV ions. It was speculated that these porous structures occur due to bubble migration towards the surface, preventing the exfoliation (surface rupture) that generally accompanies blistering at near room temperatures. Moreover, in recent years, "fuzz" formation on tungsten as a result of helium implantation has been studied due to its potential formation in the diverter region of a tokamak fusion reactor [12]. Using Helium Ion Microscopy (HIM) for site-specific irradiation and surface imaging at 30 keV, Chen et al. studied blistering mechanisms in nanocrystalline tungsten compared to coarse-grained tungsten [13]. The authors found that the onset of blistering occurred at a critical dose of  $5 \times 10^3$  ions/nm² in the coarse-grained samples, whereas no blistering occurred in the nanocrystalline samples, even at doses of up to  $1 \times 10^5$  ions/nm². HIM imaging of domed blister surfaces by the detection of secondary electrons has also revealed channeling effects, observing a reduction in secondary electron yield for regions where ion channeling occurs [14-16].

In the present work, the near-surface structural changes of tungsten upon exposure to 25 keV helium ions are investigated using a combination of site-specific implantation in a Helium Ion Microscope and various imaging/probing techniques in order to gain further insight into the interactions between ions in the keV energy range and surfaces, extending our previous studies [17, 18]. Finally, a phenomenological equation is proposed to explain the bubble formation, surface swelling and the variation in local hardness with depth that are observed experimentally.

## 2. Experimental

High purity single-crystal W(100) samples and polycrystalline tungsten in the form of  $5 \times 1$  mm disks were mechanically polished to about 1 nm RMS roughness (final step mechanical polish with a VibroMet<sup>TM</sup>), as verified by Atomic Force Microscopy (AFM). Helium implantation was then performed using the focused helium ion beam of a Zeiss ORION NanoFab Helium Ion Microscope operated at 25 keV. Appropriate beam currents were selected by varying the aperture size; the largest areas  $(10\times10~\mu\text{m}^2)$  were implanted at  $\sim100~\text{pA}$  (no aperture, beam spot size of tens of nanometers) and the smallest areas  $(2\times2~\mu\text{m}^2)$  and below) were implanted at  $\sim1~\text{pA}$  (10  $\mu$ m aperture, beam spot size  $\sim0.5~\text{nm}$ ). The helium gas pressure at the source was  $2\times10^{-6}$  Torr. The stage holding the sample during implantation was kept at room temperature and no post implantation heating was carried out. Because of the high thermal conductivity of tungsten (164 W/(m-K)) and the implant duration, it is not expected that the sample temperature increased significantly above room temperature during the implantation. The implanted areas were defined using NanoPatterning and Visualization Engine (NPVE) software (Fibics, Inc.), typically implementing a pixel dwell time of 1  $\mu$ s and pixel spacing of 0.5 nm. The total implantation dose

was varied from  $1\times10^2$  to  $1\times10^4$  ions/nm² in separate runs. All HIM imaging prior to the subsequent ex-situ analysis was performed at low dose using a beam current of  $\sim1$  pA. Optical markers close to implanted regions were added by milling cross shapes using a gallium focused ion beam (FIB) also on the ORION NanoFab instrument. The ion depth and displacements per atom (dpa) were calculated using the software Stopping and Range of Ions in Matter (SRIM). The "quick calculation" mode was used.

Surface topography changes (roughness and swelling) upon implantation were analyzed by AFM using a Digital Instruments Nanoscope III. A silicon tip with a radius of curvature of  $\sim 10$  nm was used for the imaging (image size  $256 \times 256$  pixels) and the height resolution achieved was a few angstroms. Sub-surface structural changes were then analyzed by cross-sectioning implanted regions by gallium FIB milling and imaging the cross sections by HIM. Scanning Electron Microscopy (SEM) and Electron backscatter diffraction (EBSD) analysis for grain mapping of the polycrystalline sample were performed using a dual-beam FEI Quanta instrument and Oxford EBSD software.

The mechanical properties of the implanted areas were investigated using a Hysitron TI 950 TriboIndenter with a diamond Berkovich indenter tip. For each implantation dose, the commercially available Continuous Stiffness Measurement (CSM) technique was used to evaluate the depth dependence of hardness and elastic modulus at various locations on implanted and non-implanted regions in order to validate the consistency of the results. The technique uses an oscillatory load, with a small amplitude and a high frequency superimposed on a slowly varying load by the indenter tip. This allows one to obtain a stiffness S as a function of depth using the Oliver and Pharr Method [29]. The system was calibrated against fused silica, which is a standard procedure for all nanoindentation measurements.

#### 3. Results

Figure 1a shows swelling height versus dose, as measured by AFM. The solid black circles show the data points for single-crystal W(100). A linear increase in height versus dose is observed up to a dose of  $\sim 6 \times 10^3$  ions/nm². Above a threshold dose of  $5 \times 10^3$  ions/nm², blistering starts to occur (note that the swelling height measurements are average values from non-blistered regions). In addition to previously reported measurements in [16], two more data points at  $7 \times 10^3$  and  $8 \times 10^3$  ions/nm² have been added for further linearity check. Above the threshold dose, it appears swelling starts to deviate from the above-noted linear behavior, although at the higher doses the larger error bars due to blistering may still justify a linear assumption. Data points for a polycrystalline sample for an irradiation dose of  $1 \times 10^4$  ions/nm² (red open circles) suggest that the swelling is not sensitive to crystal orientation within the experimental capability of this measurement. Of course, the AFM height measurement results are limited by the surface roughness of the sample and the error bar represents this. We find a 4 nm error on a 40 nm swelling. If the crystal orientation caused an effect, it would be smaller than the here reported values.

The boundary condition imposed by the HIM localized helium implantation performed here confines swelling to occur in the direction normal to the surface, which differs from the isotropic swelling generally discussed in the literature. In order to evaluate the influence of lateral surface constraints on the swelling behavior, a laterally unconstrained swelling experiment was designed by FIB milling trenches around the region to be implanted. This released the matrix constraints to allow unconstrained three-dimensional volume expansion of the irradiated site. The AFM height map (z-scale: -100 to 100 nm) in Fig. 1b shows the results for the constrained (top) and unconstrained case (bottom). The dose used for both was  $7 \times 10^3$  ions/nm<sup>2</sup>. Cross-sectional line profiles, avoiding blisters, suggest perhaps a slightly lower swelling height for the trenched scenario compared to the usual constrained case, within the experimental error of the measurements (see Fig. 1c and purple diamond data point added to Fig. 1a). The lower swelling height on a constrained site might be expected to reveal nanometer bubbles with a slight "cigar shape", with the long axis perpendicular to the surface. However, we do not yet have TEM data to corroborate this. Furthermore, the AFM tip of ~10 nm radius of curvature utilized in the present study unfortunately prevented us from determining the expected lateral expansion of <30 nm (accounting for the Poisson ratio influence as well) for the unconstrained implantation case.

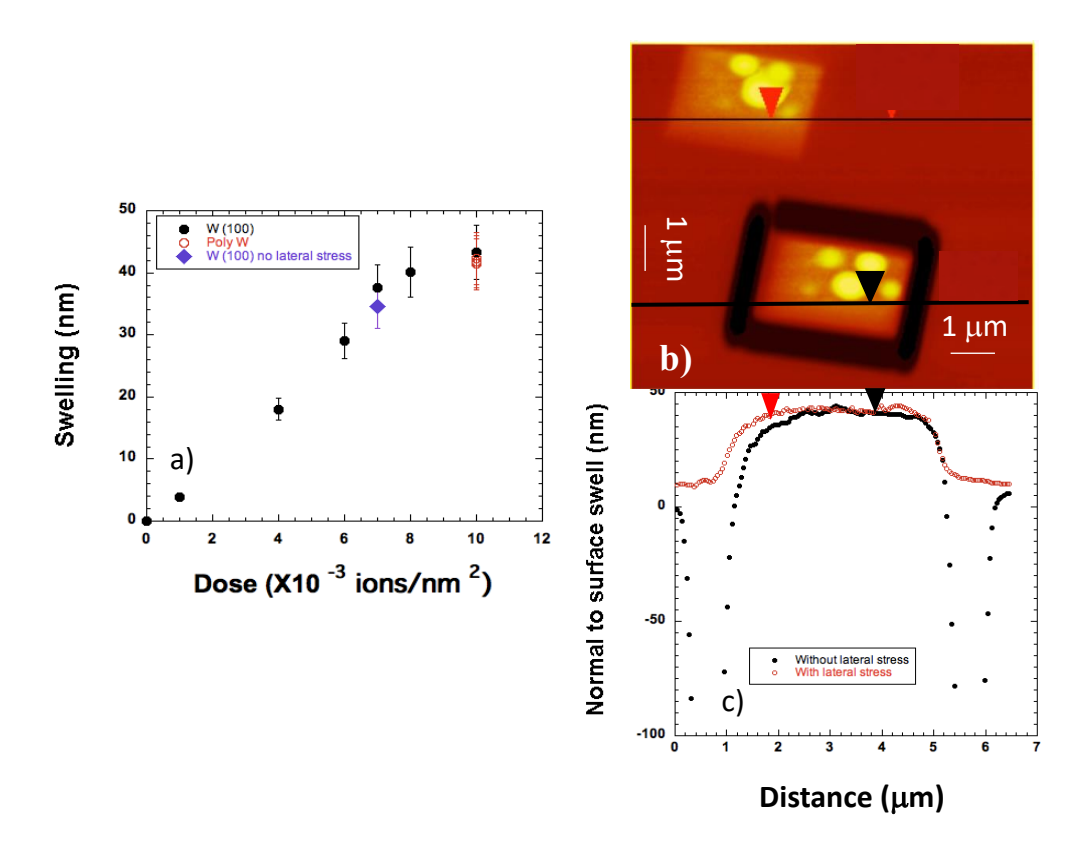


Figure 1: (a) Swelling height as a function of dose for single crystal tungsten W(100) and polycrystalline tungsten. (b) AFM height map (z-scale: -100 to 100 nm) showing unconstrained case (with FIB trenches) at the bottom, and usual constrained case at the top for the W(100) sample

using a dose of  $7 \times 10^3$  ions/nm<sup>2</sup>. (c) AFM cross-sectional height profiles across the irradiated regions marked in (b).

As noted above, exceeding a dose of 5×10³ ions/nm² leads to the formation of surface blisters (five are seen in Fig. 1b for each implanted area, with varying diameters), which were studied in detail by Transmission Electron Microscopy (TEM) in ref. [16]. Cross-sectional analysis of the blisters revealed that the depth of the crack plane inside the blister agrees reasonably well with that of the helium peak predicted from Monte Carlo Stopping and Range of Ions in Matter (SRIM) simulations. SRIM provides quick calculations producing tables of stopping powers, range and distributions of ions at specific energy in an elemental target with input of its density. The slight depth increase that was observed experimentally is attributed to the progressive decrease in material density due to helium implantation and possibly also deeper penetration of the ions due to channeling. In the following analysis the ion range is assumed to change linearly with dose. We note that the thickness of the blister shell is much greater than the ion range, due to swelling effects (i.e. the thickness of the blister shell and the depth of the crack plane are not equivalent) [16].

Figure 2 shows EBSD results and HIM images for the polycrystalline tungsten sample, where five  $2\times2~\mu\text{m}^2$  areas were irradiated with  $1\times10^4$  ions/nm². The average grain size for this region of the sample is  $\sim10~\mu\text{m}$ . In the HIM overview image (Fig. 2a), different gray levels corresponding to the individual grains are observed, indicating that HIM secondary electron channeling contrast can be used to map grain orientations, as observed elsewhere [19]. Darker grains are oriented in directions more favorable for channeling (less secondary electron emission from the surface) whereas lighter grains are oriented less favorably for channeling (more secondary electron emission from the surface). The EBSD grain orientation map of the same region (top of Fig. 2) confirms the sensitivity of HIM secondary electron imaging to the different crystal orientations. Images Fig. 2b-f show higher magnification HIM views of the five irradiated regions. Out of the five regions, that of Fig. 2c (the red-colored EBSD grain) most clearly reveals cross-shaped dark lines similar to data reported in ref [16], suggesting that the grain was oriented close to (100). In addition, for the irradiation area covering grain boundaries (Fig. 2d) blistering appears to be suppressed, as also recently reported by Chen et. al [13], showing a blister that did not extend beyond the nearest grain boundary.

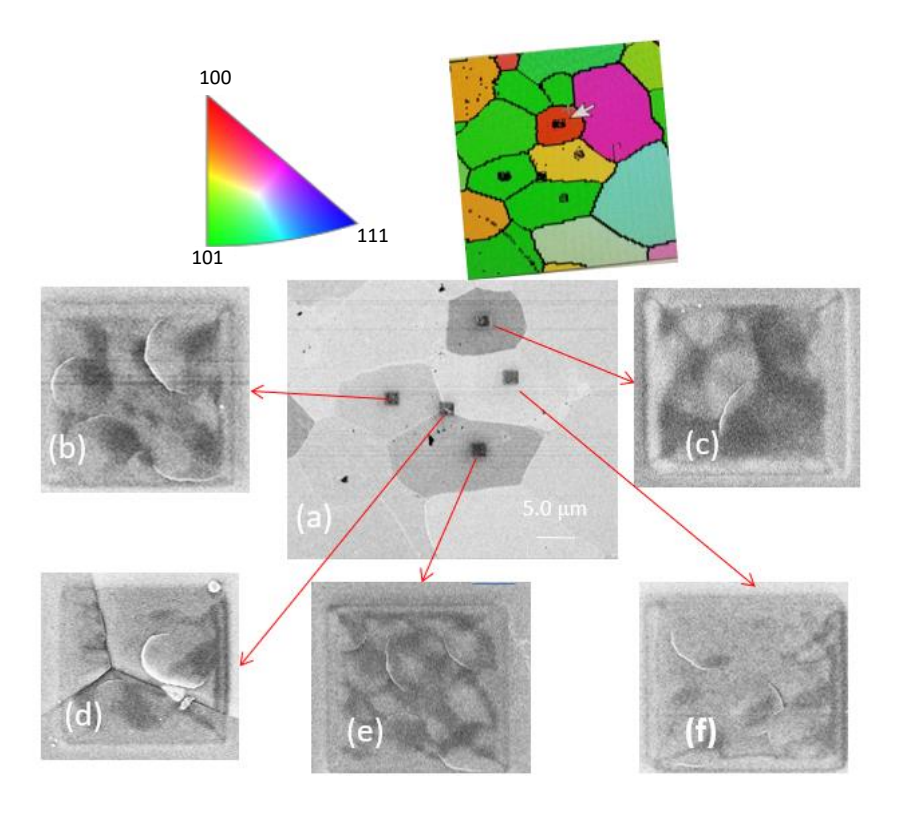


Figure 2. EBSD grain orientation map (top) and HIM images in (a)-(f) showing five  $2\times 2 \mu m^2$  regions on polycrystalline tungsten irradiated with  $1\times 10^4$  ions/nm<sup>2</sup>.

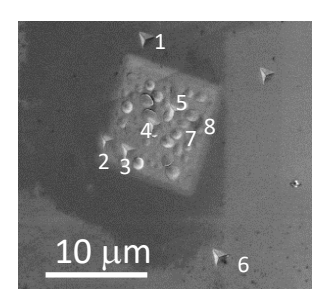
Michael [20] experimentally demonstrated that ion beam irradiation with 30 keV Ga ions can result in microstructural modification in fine grained materials. The cited work reports the formation of new grains with a channeling direction parallel to the ion beam direction. The present study, however, does not find evidence for this phenomenon using helium ions.

Figure 3 presents the reduced elastic modulus and hardness values versus penetration depth obtained by nanoindentation using the Continuous Stiffness Measurements (CSM) method on the single-crystal W(100) sample irradiated with a dose of  $6\times10^3$  ions/nm<sup>2</sup> over an area of  $10\times10$  µm<sup>2</sup>. The results for nine indents are plotted, two of which were performed outside the implanted region (indents 1, 6) and seven within the implanted region (indents 5, 7, 8 on top of blisters, and indents 2, 3, 4 on swollen regions without blisters). The annotated SEM image in Fig. 3 (top) marks the location of each indent.

In the non-irradiated case (neglecting the near-surface values from the first 20 nm), hardness decreased with increasing penetration depth, starting at ~15 GPa and asymptotically approaching ~6 GPa at deep indentation. The phenomenon that higher values of hardness are recorded for shallower indents is explained by the well-known indentation size effect, where hardness increases with decreasing indentation depth, since dislocations generated beneath the indenter give rise to strain gradients that cause enhanced hardening [21-23]. In general, for regions inside the implanted

area that were not on blisters, the hardness values were higher than for unirradiated neighboring regions, reaching a maximum at around 40-50 nm depth. In contrast, indents on the blisters themselves generally gave much lower hardness values at shallow penetration, either passing through a maximum before converging to around 6 GPa for the deeper indents or approaching around 6 GPa monotonically. Clearly, interpreting the hardness values from blistered regions based on a simple semi-infinite media approximation would be erroneous.

The reduced modulus of the unirradiated regions (neglecting the initial 20 nm) is measured to be ~330 GPa, in good agreement with values reported in the literature [22]. On the irradiated area but off the blisters, the value is reduced to ~270 GPa. In contrast, indentations on blisters gave reduced modulus values that increased gradually with indentation depth, rising toward the unirradiated values asymptotically as the indentation depth is increased.



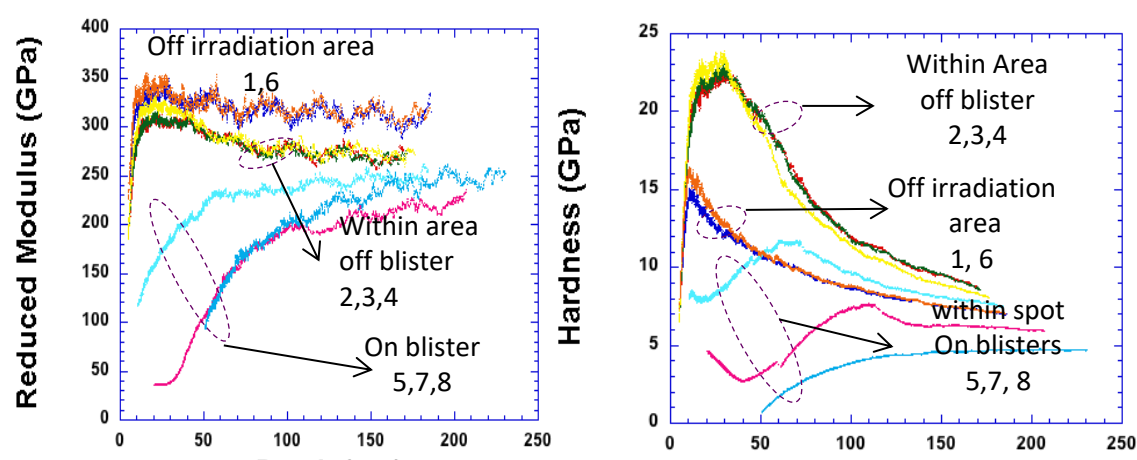


Figure 3. SEM image of single-crystal W(100) irradiated over an area of  $10 \times 10$   $\mu m^2$  with  $6 \times 10^3$  ions/nm<sup>2</sup> - eight subsequently indented regions are marked. The corresponding plots of reduced elastic modulus and hardness versus indentation depth are shown.

## 4. Analysis

The following discussion presents an analytical approach to quantify swelling as a function of helium dose and the related hardness changes.

The projected range,  $R_p$ , of implanted ions as a function of ion energy, taking into account both nuclear as well as electronic interactions between the incident ions and target atoms, was formulated by Schiott [24] as follows:

$$R_{p}(nm) = 10 \frac{C_{i}(m)A_{2}(z_{1}^{2/3} + z_{2}^{2/3})^{1/2}}{z_{1}z_{2}r(g/cm^{3})} E(keV)$$
(1)

where the subscripts 1 and 2 denote the incident ions and target atoms, respectively. The atomic number of the target is given by  $A_2$ , the atomic masses of the incident ions and target atoms are  $z_1$ ,  $z_2$ , and  $\rho$  is the density of the target.  $C_i(\mu)$  is a proportionality constant depending on the mass number ratio of the target atoms to the incident ions ( $\mu = A_2/A_1$ ). For helium ions of energy of 25 keV incident on a tungsten target, the average projected range calculated from Eq. 1 is 60 to 70 nm. Monte Carlo "Stopping and Range of Ions in Matter" (SRIM) simulations, which are based on the same type of relation, give a similar depth. However, the experimentally determined thickness of the blister shells revealed by TEM cross-sectional analysis performed in [16] is a factor of two larger than the projected ion range calculated from Eq. 1. The thickening is assumed to be due to swelling induced by the implanted helium nanobubbles and the formation of nanocracks, as discussed in reference [16].

Clearly, volumetric swelling of an irradiated area is constrained by the surrounding, non-implanted regions. Therefore, the only way the volume expansion can be accommodated is by an increase in surface height. Local implantation causes a lateral constraint that in turns generates a stress gradient, which could lead to the upwards swelling observed. However, the FIB-milled trenches (Fig. 1b-c) presented earlier released this lateral constraint, resulting in only slightly less swelling in the upwards direction (within the error of the measurement). Therefore, lateral stress cannot be

a major contributing factor in the upward swelling. Most likely the initial interstitial and vacancy flow driven by local conditions drive the swelling phenomenon.

It appears that neither swelling nor blistering depend on crystal orientation for the orientations investigated in Figure 2, as the same degree of swelling and threshold dose for blistering are observed regardless of orientation. However, core orientations such as <111> are not investigated here. Recent work by Fan and co-authors [33] suggests that particularly the <111> orientation may change the outcome. However, since we do observe a difference in channeling contrast, as expected for different orientations [19], this may also contribute to increasing the implantation depth, even though not significantly.

From the experimental observations of blister formation with increasing dose it is clear that there is plastic deformation at the surface with eventual fracture at the periphery of the blister. At the point of plastic deformation, at equilibrium, the force balance requires [10]

$$\pi r^2 P = 2\pi r R_P Y \tag{2}$$

The blister radius *r* can then be obtained from:

$$r = \frac{2R_P Y}{P} \tag{3}$$

where  $R_p$  is the projected range of ions in the solid, Y is the yield strength of the sample (550 MPa [24]) and P is the helium gas pressure inside the blister cavity. Assuming a typical blister with r=500 nm,  $R_p=70$  nm, Eq. 3 gives a helium gas pressure inside the cavity causing the blister of ~150 MPa. With the maximum height of the cavity measured as h=60 nm (by AFM) and assuming a simple spherical cap volume for the cavity, the volume of the cavity is estimated as  $V_{cav}=\frac{\pi}{6}h(3r^2+h^2)=2.37x10^{-20}$  m<sup>3</sup>. Assuming the cavity contains helium at equilibrium pressure and the ideal gas law applies, the number of helium atoms within the cavity is:

$$N_{He} = \frac{pV_{cav}}{kT} = 9 \times 10^9 \tag{4}$$

At the maximum dose of  $1\times10^4$  ions/nm<sup>2</sup>, this means that less than 10% of the implanted atoms ended up in the blister cavity while the rest are dispersed likely as small bubbles contributing to the uniform swelling behavior observed by AFM. Indeed, detailed TEM analysis of similar samples showed significant nanobubbles dispersed within the blister shell [16]. Most likely, the suggested numerical value for  $N_{He}$  in Eq. 4 is exaggerated, since the yield strength of 550 GPa used in Eq. 3 is for an unirradiated sample. The yield strength is expected to reduce with dose due to the increase in porosity near the surface of the sample.

It is generally accepted that helium atoms implanted into metals can be rapidly displaced from their equilibrium positions to form helium atom/vacancy complexes [26] that are in term mobile

and can recombine to form bubbles. They also act as sinks for attracting further complexes, resulting in further bubble growth. As the bubble size increases, however, the mobility of the helium atom/vacancy complexes gradually diminishes and bubbles mostly increase in size by absorbing complexes. Currently, a detailed mechanism for the process of bubble nucleation and growth in metals is still outstanding.

In the following paragraphs an attempt is made to formulate the bubble nucleation and growth process to qualitatively explain the hardness observed on the irradiated area. More sophisticated approaches can be considered using computational efforts but are not part of this work.

To begin, we consider the simple assumption of an implanted helium distribution based on a Gaussian profile:

$$n_0(x) = \frac{D}{\sqrt{2\pi}\Delta R_P} exp\left[-\frac{(x-R_P)^2}{2\Delta R_P^2}\right]$$
 (5)

where x is the implant depth, D is the helium ion dose [ions/nm<sup>2</sup>],  $R_p$  is the projected ion range and  $\Delta R_P$  is its standard deviation.

At high doses, however, where sputtering and swelling take place simultaneously, the profile must be modified as follows:

First, to account for sputtering, the change in the helium profile in time dt and at depth x' from the original surface (x=x'-vt), the distribution can be expressed as [27]:

$$dn_0(x') = \frac{j}{\sqrt{2\pi}\Delta R_P} exp\left[-\frac{(x'-vt-R_P)^2}{2\Delta R_P^2}\right] dt$$
 (6)

where j is the helium ion flux (ions/nm<sup>2</sup>-s), v is the speed of surface motion by sputtering.  $N_{\theta}$  is the theoretical atomic density of tungsten (63 atoms/nm<sup>3</sup>):

$$N_0 = \frac{jS}{\nu} \tag{7}$$

where S is the sputtering coefficient describing the moving x coordinate of the surface due to sputtering during the implantation.

Adopting a change in variables as follows:

$$\tau = \left[ -\frac{(x - vt - R_P)}{\sqrt{2}\Delta R_P} \right] \tag{8}$$

And by using the definition of the error function:

$$\int \exp(-\tau^2) d\tau = \sqrt{\frac{\pi}{4}} \operatorname{erf}(\tau) \tag{9}$$

The integration of Eq. 5 results in a helium density profile expressed as:

$$n_{He} = \frac{N_0}{2S} \left[ erf \left\{ \frac{x + \frac{DS}{N_0} - R_P}{\sqrt{2}\Delta R_P} \right\} - erf \left\{ \frac{x - R_P}{\sqrt{2}\Delta R_P} \right\} \right]$$
 (10)

Second, in addition to sputtering, the density of the target will be reduced due to the aforementioned buildup of nano-sized cavities. At high implantation dose and due to the fact that the solubility of helium in tungsten is limited and the diffusion coefficient of helium atoms in tungsten at room temperature is high ( $\sim 4 \times 10^{-6}$  cm<sup>2</sup>/s), the helium atoms will quickly combine with vacancies to form helium atom/vacancy complexes at low doses, perhaps as low as  $\sim 10^2$  ions/nm<sup>2</sup>, since swelling was not detected for this dose by AFM. Further increase in dose allows additional helium to join the complexes through diffusion, expanding their size to small bubbles. These bubbles, however, are still mobile and can combine to further increase their size. The larger the size, however, the lower the mobility of the bubbles becomes. At  $1 \times 10^4$  ions/nm<sup>2</sup>, the bubble size asymptotically reaches  $\sim 1$  to 2 nm in diameter, as TEM analysis suggests [16]. The bubble formation process thus significantly contributes to the decrease in density of the host tungsten, which in turn results in increasing the ion projection range,  $R_P$ 

Based on the AFM results in Fig. 1a, showing only slight non-linearity at high doses, it is still assumed, for simplicity, a linear increase in  $R_P$  with dose, starting at 60 nm for theoretical target density and rising to  $\sim 70$  nm at the maximum dose of  $1\times10^4$  ions/nm<sup>2</sup>.

The helium bubble concentration profile is then assumed to have the same profile as the implanted helium atom profile, represented in Eq. 10, but with a lower concentration by a factor of  $\eta$  to account for the collection of helium atoms that are associated with any given bubble. The helium bubble concentration profile can then be written as:

$$n_{bubble}(x,D) = \eta \frac{N_0}{2S} \left[ erf \left\{ \frac{x + \frac{DS}{N_0} - R_P}{\sqrt{2}\Delta R_P} \right\} - erf \left\{ \frac{x - R_P}{\sqrt{2}\Delta R_P} \right\} \right]$$
(11)

For material such as tungsten, with a small sputtering coefficient ( $\sim 4 \times 10^{-2}$  sputtered atoms/ion), Eq. 11 can be simplified as:

$$n_{bubble}(x, D) \approx \eta \frac{D}{\sqrt{2\pi}\Delta R_P} exp\left[-\frac{(x-R_P)^2}{2\Delta R_P^2}\right]$$
 (12)

 $\eta$  can be estimated from an evaluation of the porosity using TEM cross-sectional analysis at a measured depth.

The above equation provides a simple means to characterize the helium bubble distribution and thus interpret the AFM measurements of height increase with dose as shown below.

Following the Indentation Size Effect (ISE) model put forward by Nix and Gao [21], which considers the dislocations required to accommodate the geometry of plastic deformation, the hardness variation with depth is written as:

$$\frac{H}{H_0} = \sqrt{1 + \frac{x^*}{x}} \tag{13}$$

where H is the hardness at a given indentation depth x,  $H_0$  is the hardness at large depth and  $x^*$  is a characteristic length depending on the indentation tip geometry as well as the shear modulus. Using Eq. 13, the present experimental results of  $H^2$  vs. I/x evaluate the applicability of the Nix and Gao model (Fig. 4). The unirradiated material behaves linearly in the Nix-Gao plot as expected and suggests a value of  $x^*$  of 25 nm and an  $H_0$  of 6 GPa. Similar results are obtained for the material implanted using the low dose of  $10^2$  helium ions/nm², giving  $x^*$  of 37 nm and  $H_0$  of 7.2 GPa, slightly deviating from the unirradiated results due to helium implantation as indicated in reference [27]. At higher dose, however, where helium bubbles build up and even blistering occurs, the behavior changes and vastly deviates from this simple relationship. Fig. 5 shows that hardness passes through a maximum at an indentation depth of  $\sim$  50-70 nm and then the material gradually softens at deeper penetration depths. This unusual behavior is explained by the fact that an indenter causes a plastic zone of at least four times the indentation depth [33,34]. Therefore, an indentation that is 50 nm deep, for example, samples a zone to a depth of  $\sim$  200 nm. To simplify the analysis, data from the first 20 nm of indentation depth (due to surface and roughness effects) are excluded.

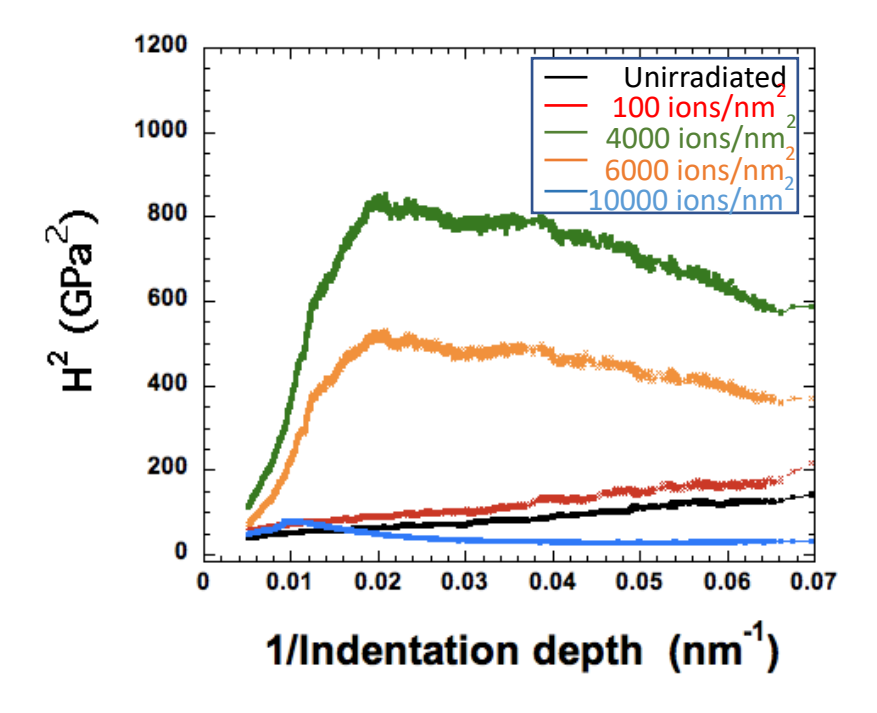


Figure 4: Experimentally-determined hardness versus depth for W(100) sample irradiated with different doses of helium ions plotted in the form of Nix-Gao plots.

Helium bubbles in general lead to hardening of the material due to the dislocation obstacle mechanism. The change in polycrystalline yield strength and its hardness can be calculated, through Tabor's relation, using the Friedel-Kroupa-Hirsch (FKH) equation for weak obstacles [29, 30]:

$$\Delta H = 3\Delta \sigma = 3/8M\mu b dn_{obs}^{2/3} \tag{14}$$

where  $n_{obs}$  is the obstacle density,  $\mu$  is the shear modulus (130 GPa for tungsten), b is the Burgers vector (we use  $b = \frac{a}{2}\sqrt{3}$  for slip in the [111] direction with a being the lattice constant), M is the Taylor factor (3.06 for equiaxed BCC and FCC metals), and d is the bubble diameter.

However, as shown in Fig. 4, a significant drop in hardness is observed for a given depth as the helium dose is increased from  $4\times10^3$  to  $6\times10^3$  ions/nm<sup>2</sup>, which can be attributed to an increase in porosity. Therefore, the sample can be treated as a porous metal [32], with  $\rho^*$  being the new density (with porosity) and  $\rho$  the solid density.

The elastic modulus can then be presented as:

$$\frac{E^*}{E} = C_0 \left(\frac{\rho^*}{\rho}\right)^n \tag{15}$$

where E is the elastic modulus of the dense material,  $E^*$  is the elastic modulus of the porous material, and  $C_0$  and n are constants depending on the nature of the pores (open or closed porosity). Presenting Eq. 15 in terms of porosity yields:

$$\frac{E^*}{E} = C_0 (1 - P)^n \tag{16}$$

Similar equations exist for the change in yield strength and hardness, with a different parameter labeled here as  $C_1$ :

$$\frac{\sigma^*}{\sigma} = \frac{H^*}{H} = C_1 (1 - P)^n \tag{17}$$

For materials with a density ratio of more than 0.3, n is found to be close 2.  $C_0$  and  $C_1$  are coefficients that are material and structure dependent.

From Eq. 12 the depth-dependent porosity can be formulated as:

$$P(x,D) \approx \frac{V_{bubble}}{V_w N_0} \eta \frac{D}{\sqrt{2\pi}\Delta R_P} exp\left[-\frac{(x-R_P)^2}{2\Delta R_P^2}\right]$$
 (18)

where  $V_w = 1.07 \times 10^{-2} \ nm^{-3}$  is the volume per atom of W,  $N_0 = 62.9 \ nm^{-3}$  is the bulk atomic density of W.

The final equation that accounts for obstacles and porosity effects is expressed as:

$$H(x,D) = H_0 \sqrt{1 + \frac{x^*}{x}} \{ [C_1(1-P)^2] + C_2[P]^{2/3} \}$$
 (19)

where  $C_2$  is a parameter introduced for fitting the data that accounts for the coefficients of obstacle density (assumed here equal to bubble density) in Eq. 12, as well as the coefficients in Eq 18. Eq. 19 suggests that there are two contributing factors to the change in hardness: First, the formation of bubbles generating porosity in the material that contributes to the decrease in hardness (first term inside the bracket). Second, the bubbles at the same time assist in suppressing the dislocation movement and, therefore, increase the hardness (second term inside the bracket). The competition between these two factors facilitates the macroscopic observation of the behavior of hardness versus depth that goes through a maximum as the dose increased.

To fit the H(x,D) data presented in Fig. 4, Eqs. 12 and 19 are combined with optimized parameters of :

$$\Delta R_p = 0.45 R_p$$
,  $C_2 = 1467 \left(1 - \frac{D}{10^4}\right)$ ,  $C_1 = 1$  and:

$$R_p(nm) = 60 + \frac{10D}{10^4} \tag{20}$$

 $\eta = 0.0005$  is deduced from porosity analysis of our previous TEM studies [16] at the depth of  $R_P$ .  $C_1$  is not considered simply as a constant as expressed in Eq. 17, but assumed to be dose dependent. It accounts for nanocrack formation between the bubbles for doses above  $10^4$  ions/nm<sup>2</sup> [16]. These cracks contribute to absorbing implanted helium instead of forming new bubbles. The results of fitting the experimental results are shown in Fig. 5.

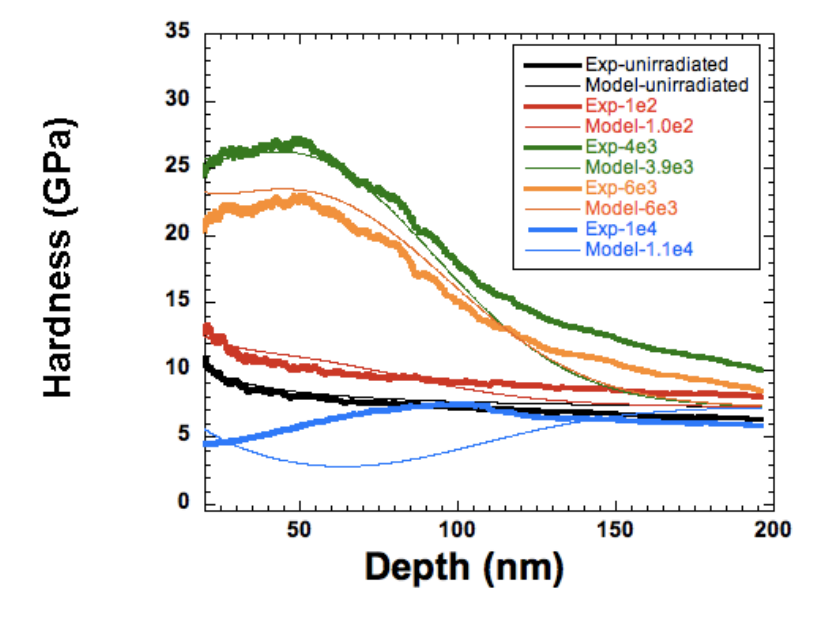


Fig. 5: Plot of hardness versus indentation depth, comparing the experimental nanoindentation data with the model data.

The simple model presented provides a reasonable fit to the experimental results. Its simple explanation provides the reasoning behind the trend of hardness passing through a maximum as the dose increased. However, at the maximum dose of 10<sup>4</sup> ions/nm<sup>2</sup> the hardness behavior with depth can no longer be explained by the model due to the fact that most of the surface is covered with blisters and hence flexure of the shells will strongly influence the hardness values obtained in the nanoindentation tests.

The one-dimensional swelling in the x direction, perpendicular to the surface is:

$$\Delta X(D) = \int_{0 \ nm}^{200 \ nm} n_{bubble}(x, D) \times V_{bubble} \ dx \tag{21}$$

Plotting the results from Eqs. 12 and 21 and comparing with the AFM measurements (Fig. 1a) shows fair agreement between the measurements and the analytical model, as shown in Fig. 6. It is important to note that Eq. 21 assumes swelling starts at any value of dose greater than zero, i.e., interstitial He atoms immediately form He/vacancy complexes with high enough mobility to grow. In practice, there is a threshold dose below which the assumption of immediate formation of bubbles to 1-2 nm diameter is no longer valid. Furthermore, it is likely that there exists a dose value for which the He atoms remain at interstitial sites without any cluster formation. However, the threshold dose is less than  $1 \times 10^3$  ions/nm<sup>2</sup>, which is the lower limit of our AFM measurements. Therefore, a linear extrapolation passing through zero coordinates for doses less than  $1 \times 10^3$  ions/nm<sup>2</sup> is not justified.

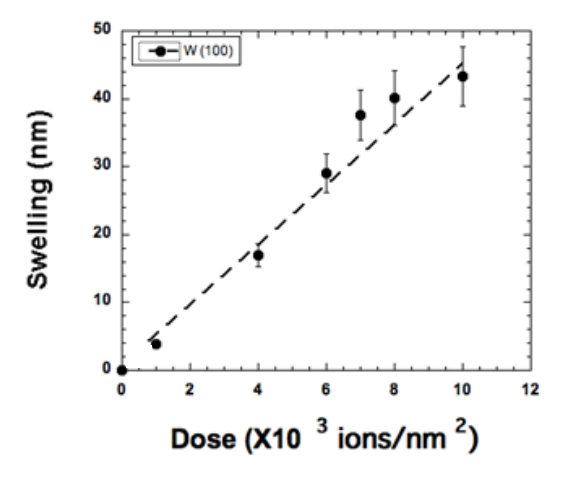


Figure 6: Modeled vertical swelling behavior versus dose computed from Eqs. 12 and 13 (dashed line), compared with the experimental AFM results from Fig. 1a.

## 5. Summary and Conclusion

Our combinatorial characterization approach for studying high-dose near-surface helium implantation enabled us to shed light on the threshold dose for helium blistering on tungsten and on the resulting mechanical properties. We were able to show that the elastic modulus is reduced with increasing helium dose and that the hardness values first increase and then decrease. We show that this is due to the fact that helium bubbles are hardening defects, but in large concentration cause the material to behave more like a foam, due to the large amount of open volume. The open volume can easily be characterized by swelling, and therefore hardening and swelling can be rated to each other. Furthermore, we establish a simple yet rather effective analytical way of describing the hardening of a material with increasing helium dose, considering helium bubble formation and well-known hardening laws. This analytical method is put to the test and was found to fit well with the data. Future studies of other materials will enable further investigation of the validity of this simple analytical model.

Furthermore, we find that the grain orientation does not have a significant effect on swelling in our study. More specifically, any effect of grain orientation is smaller than the error originating from the surface roughness.

We find that releasing the material's stress in the surrounding matrix by FIB trenching does not affect the swelling within the error of our measurement. This agrees well with a previous study of the residual stress in helium implanted materials, i.e. that the residual stress does not exceed the yield stress and the material simply flows [34]. In fact, this further shows that it cannot be the lateral stress buildup due to swelling that leads to blistering, but must be other phenomena such as gas bubble pressure.

Surface degradation due to helium irradiation is an important issue for fusion energy and this work sheds light on the degradation mechanism. Finally, it places a boundary on the maximum dose a surface can accommodate before significant surface degradation by blistering occurs.

## Acknowledgement

Financial support for this research was provided by NSF-DMR Program # 1807822. The authors thank the Biomolecular Nanotechnology Center (BNC) at UC Berkeley for making the Zeiss ORION NanoFab Helium Ion Microscope and the FEI Quanta 3D FEG Dual Beam FIB available to users. The authors also thank David M. Frazer for useful discussions and suggestions.

### References

- [1] Dwaipayan Dasgupta, Robert D. Kolasinski, Raymond W. Friddle, Lin Du, Dimitrios Maroudas, Brian D. Wirth, "On the origin of 'fuzz' formation in plasma facing materials" *Nucl. Fusion* 59 (2019) 086057 (11pp). https://iopscience.iop.org/article/10.1088/1741-4326/ab22cb/meta
- [2] R. E. Nygren, L. Youchison, B. D. Wirth, L. L. Snead, A new vision of plasma facing components, <u>Fusion Engineering and Design</u>, 109–111, Part A, (2016), 192-200. https://www.sciencedirect.com/science/article/pii/S0920379616302277
- [3] H. Bolt, V. Barabash, G. Federici, J. Linke, A. Loarte, J. Roth, and K. Sato, Plasma facing and high heat flus materials-needs for ITER and beyond, *J. Nucl. Mater.* 307–311, 1, (2002) 43–52. https://doi.org/10.1016/S0022-3115(02)01175-3
- [4] V. K. Alimov, Y. Hatano, B. Tyburska-Puschel, K. Sugiyama, et al., Deuterium retention in tungsten damage with W ions to various damage levels, *J. Nucl. Mater.* 441 (2013) 280-285. https://doi.org/10.1016/j.jnucmat.2013.06.005
- [5] W. Primak and J. Luthra, Radiation Blistering: Interferometric and Microscopic Observations of Oxides, Silicon, and Metals, J. App. Phys. 37 (1966) 2287. <a href="https://doi.org/10.1063/1.1708805">https://doi.org/10.1063/1.1708805</a>
- [6] M. Kaminsky, Adv. Mass Spectrometry 3 (1964) 69.
- [7] R. D. Daniels, Correlation of Hydrogen Evolution with Surface Blistering in Proton-Irradiated Aluminum, *J. Appl. Phys.* 42 (1971) 417. https://doi.org/10.1063/1.1659613
- [8] R. S. Nelson, The sputtering of metals with noble gas ions; an experiment to determine the fate of the injected gas and its influence on the sputtering process, *Phil. Mag.* 9/98 (1964) 343-347. https://doi.org/10.1080/14786436408229198
- [9] W, Bauer, G. J. Thomas, Helium release and electron-microscopy of helium-implanted palladium, *J. Nucl. Mat.* 42 (1972) 96-100. https://doi.org/10.1016/0022-3115(72)90012-8
- [10] S. K. Erents, G. M. McCracken, Blistering of molybdenum under helium ion bombardment, *Rad. Effects* 18 (1973), 191-198. <a href="https://doi.org/10.1080/00337577308232121">https://doi.org/10.1080/00337577308232121</a>
- [11] B. B. Cipiti, G. L. Kulcinski. Helium and deuterium implantation in tungsten at elevated temperatures, *J. Nuc. Mater.*, 347 (2005) 298-306. <a href="https://doi.org/10.1016/j.jnucmat.2005.08.009">https://doi.org/10.1016/j.jnucmat.2005.08.009</a>
- [12] T. J. Petty, M. J. Baldwin, M. I. Hasan, R. P. Doerner, J. W. Bradley, Tungsten 'fuzz' growth re-examined: the dependence on ion fluence in non-erosive and erosive helium plasma, *Nucl. Fusion* 55 (2015) 093033. <a href="https://doi.org/10.1088/0029-5515/55/9/093033">https://doi.org/10.1088/0029-5515/55/9/093033</a>
- [13] Z. Chen, L.-L. Niu, Z. Wang, L. Tien, L. Kecskes, K. Zhu, Q. Wei, A comparative study on the in situ helium irradiation behavior of tungsten: Coarse grain vs. nanocrystalline grain, *Acta Mater.*, 147 (2018) 100-112. https://doi.org/10.1016/j.actamat.2018.01.015
- [14] V. Veligura, G. Hlawacek, R. van Gastel, H. J. W. Zandvliet, B. Poelsema, Channeling in He-ion microscopy: Mapping of crystal orientation, *Beilstein J. Nanotechnol.* 3, (2012) 501-506. <a href="https://doi.org/10.3762/bjnano.3.57">https://doi.org/10.3762/bjnano.3.57</a>
- [15] V. Veligura, G. Hlawacek, R. P. Berkelaar, R. van Gastel, H. J. W. Zandvliet, B. Poelsema, Digging gold: keV He+ ion interaction with Au, *Beilstein J. Nanotechnol.* 4, (2013) 453-460. https://doi.org/10.3762/bjnano.4.53
- [16] F. I. Allen, P. Hosemann, M. Balooch, Key mechanistic features of swelling and blistering of helium-ion-irradiated tungsten, Scr. Mater. 178 (2020) 256-260 https://doi.org/10.1016/j.scriptamat.2019.11.039
- [17] M. V. Ambat, D. M. Frazer, M. P. Popović, M. Balooch, S. Stevenson, A. Scott, J. Kabel, P. Hosemann, Roughening and swelling of high dose He-ion implantation in different materials, *JOM* 72 (2020), 170–175. https://doi.org/10.1007/s11837-019-03869-y

- [18] Y. Yang, D. Frazer, M. Balooch, P. Hosemann, <u>Irradiation damage investigation of helium implanted polycrystalline copper</u>, *J. Nucl. Mater.* 512 (2018), 137–143. https://doi.org/10.1016/j.jnucmat.2018.09.022
- [19] G. Hlawacek, V. Veligura, R. van Gastel and B. Poelsema, Channeling and Backscatter Imaging, In: Hlawacek G., Gölzhäuser A. (eds) "Helium Ion Microscopy", NanoScience and Technology. Springer, Cham, 2016, pp. 205-224. https://doi.org/10.1007/978-3-319-41990-9 9
- [20] J. R. Michael, "Focused ion beam induced microstructural alterations: texture development, grain growth, and intermetallic formation." Microscopy and Microanalysis 17.3 (2011): 386-397.
- [21] W. D. Nix, H. Gao, Indentation size effects in crystalline materials: A law for strain gradient plasticity, J. Mech. Phys. Solids 46 (1998) 411-425 <a href="https://doi.org/10.1016/S0022-5096(97)00086-0">https://doi.org/10.1016/S0022-5096(97)00086-0</a>
- [22] Y. Huanga, F. Zhang, K.C. Hwang, W.D. Nix, G.M. Pharr, G. Feng, A model of size effects in nano-indentation, J. Mech. Phys. Sol. 54 (2006) 1668-1686. https://doi.org/10.1016/j.jmps.2006.02.002
- [23] M. Rester, C. Motz, R. Pippan, Where are the geometrically necessary dislocations accommodating small imprints? J. Mater. Res. 24 (2009) 647-651. <a href="https://doi.org/10.1557/jmr.2009.0131">https://doi.org/10.1557/jmr.2009.0131</a>
- [24] H. E. Schiøtt, Approximations and interpolation rules for ranges and range stragglings, *Rad. Effects* 6 (1970) 107. https://doi.org/10.1080/00337577008235052
- [25] Kravchenko, V.S., Sheina, I.V., Gnuchev, V.S. *et al.*, Temperature dependence of the yield strength of tungsten with different microstructures, *Strength Mater* **11**, (1979) 175–178. <a href="https://doi.org/10.1007/BF00768229">https://doi.org/10.1007/BF00768229</a>
- [26] D. Perez, L. Sandoval, S. Blondel, B. D. Worth, B. P. Uberuaga, A. F. Voter, The mobility of small vacancy/helium complexes in tungsten and its impact on retention in fusion-relevant conditions, Sci. Rep. 7, 2522 (2017). https://doi.org/10.1038/s41598-017-02428-2
- [27] Tomita, K. Masumori, Fluence and temperature-dependence of sputtering yield by 25 keV He ion bombardment on tungsten and niobium, *Nucl. Instr. Meth. Phys. Res. B*, 39 (1989), 95-98. https://doi.org/10.1016/0168-583X(89)90748-9
- [28] S. Krimpalis, K. Mergia, S. Messoloras, A. Dubinko, D. Terentyev, K. Triantou, J. Reiser, G. Pintsuk, Comparative study of the mechanical properties of different tungsten materials for fusion applications, Phys. Scr. 170 (2017) 014068. https://doi.org/10.1088/1402-4896/aa9292
- [29] W. C. Oliver and G. M. Pharr, An improved technique for determining hardness and elastic modulus using load and displacement sensing indentation experiments, *J. Mater. Res.* (1992) 1564-1583. https://doi.org/10.1557/JMR.1992.1564
- [30] F. Kroupa, P. B. Hirsch, Elastic interaction between prismatic dislocation loops and straight dislocations, Discuss. Faraday Soc. 38 (1964), 49 <a href="https://doi.org/10.1039/df9643800049">https://doi.org/10.1039/df9643800049</a>
- [31] S. Jiang and Z. Wang, Effect of Annealing on Microstructures and Hardening of Helium–Hydrogen– Implanted Sequentially Vanadium Alloys, *Nanoscale Research Letters* 13 (2018), 72 <a href="https://doi.org/10.1186/s11671-018-2485-6">https://doi.org/10.1186/s11671-018-2485-6</a>
- [32] L. J. Gibson, M. F. Ashby, The mechanics of three-dimensional cellular materials, Proc. R. Soc. Lond. A 382 (1982), 43-59. <a href="https://doi.org/10.1098/rspa.1982.0088">https://doi.org/10.1098/rspa.1982.0088</a>
- [33] C. Fan, C. Li, C. M. Parish, Y. Katoh, X. Hu; Acta Mat. 203 (2021) 116420.

[34] P. Hosemann, M. Sebastiani, M. Z. Mughal, X. Huang, A. Scott and M. Balooch, Quantifying residual stress in Helium-implanted surfaces and its implication for blistering" JMR, 36 (2021) 2349-2356.